Monthly Notices of the ROYAL ASTRONOMICAL SOCIETY

MNRAS **549**, 1–12 (2026)
Advance Access publication 2026 June 3

https://doi.org/10.1093/mnras/stag1042

Simulation-based parameter space for shock in transonic, sub-Keplerian accretion flow onto non-rotating black holes

Aishi Dasadhikary[1★] and Sudip K. Garain[1,2★]

[1]Department of Physical Sciences, Indian Institute of Science Education and Research Kolkata, Mohanpur, Nadia, WB-741246, India
[2]Center of Excellence in Space Sciences India, Indian Institute of Science Education and Research Kolkata, Mohanpur, Nadia, WB-741246, India

Accepted 2026 June 2. Received 2026 May 17; in original form 2026 April 1

ABSTRACT

Non-dissipative, transonic, sub-Keplerian accretion flow on to black holes is characterized by two conserved parameters: specific energy and specific angular momentum of the flow. For certain range of these parameters, the accretion flow shows shock formation and the post-shock matter forms a boundary layer which is believed to shape the radiative properties of the accretion disc. In this work, we identify the parameter space for shock in such accretion flows using multidimensional numerical simulations around non-rotating black holes and demonstrate that the shock formation parameter space is much larger than the analytically calculated one. We also find the boundary layer to be dynamic for a significant part of this parameter space and self-consistently produce outflow from the accretion disc.

Key words: accretion, accretion discs – hydrodynamics – shock waves – methods: numerical – stars: black holes.

1 INTRODUCTION

Black hole accretion solutions are necessarily transonic. It has been shown that general solutions of non-dissipative transonic accretion flows are described by two conserved parameters, namely, the specific (per unit mass) energy ϵ and the specific angular momentum l (J. Fukue 1987; S. K. Chakrabarti 1989, 1990). The solution with non-zero ϵ but zero l leads to the well-known spherically symmetric, Bondi accretion solution (H. Bondi 1952). With increasing l, the axisymmetric accretion flow experiences increasing outward centrifugal force. This results in the formation of a potential barrier close to the black hole, very much similar to what is observed in studying the non-radial motion of a test particle around black holes (C. W. Misner, K. S. Thorne & J. A. Wheeler 2017; S. L. Shapiro & S. A. Teukolsky 1983). If the flow has sufficient energy to overcome the barrier, accretion on to black holes is possible. Because of this potential barrier, accreting matter does not achieve a monotonically increasing magnitude of radial velocity profile. Rather, the velocity profile shows a dip close to the black hole. For certain ranges of l and ϵ, the accretion flow can even develop a shock.

Since the conceptualization of the shock formation in the axisymmetric accretion flow, several analytical and numerical studies have been carried out to investigate its formation, stability, flow parameter dependence, etc. An analytical solution aims to find the radial profile of accretion flow variables (e.g. velocity, density, and pressure) under the assumption of a thin, conical or constant height flow geometry, or for a thick flow under vertical equilibrium (S. K. Chakrabarti 1989, 1990; S. K. Chakrabarti & D. Molteni 1993a; S. K. Chakrabarti & S. Das 2001). The shock location is found by Rankine–Hugoniot (RH) analysis, suitably performed for these model flows. In numerical simulation, the solution of time-dependent fluid dynamic equations using suitable matter inflow boundary conditions determines the flow profile. Inflowing fluid variables may be computed using the above-mentioned analytical methods. For suitable parameters, the numerical solution self-consistently identifies the shock solution. Comparison between model-based analytical and numerical solutions shows very good agreement between the two methods (S. K. Chakrabarti & D. Molteni 1993a; D. Molteni, D. Ryu & S. K. Chakrabarti 1996; S.-J. Lee, D. Ryu & I. Chattopadhyay 2011; S. K. Garain & J. Kim 2023; S. Debnath, I. Chattopadhyay & R. K. Joshi 2024). Several general relativistic (GR) hydrodynamics simulations (J. Kim et al. 2017, 2019; S. K. Garain 2025) also demonstrate such agreement. Numerical simulations, additionally, allow us to study the long-time stability of the shock solutions in multiple dimensions.

Shock formation in the transonic, axisymmetric accretion disc plays an important role in interpreting observed high-energy radiation from several black hole X-ray binaries. The sub-Keplerian component in a two-component advective flow (TCAF; S. Chakrabarti & L. G. Titarchuk 1995) undergoes a shock transition. The shock makes the post-shock flow geometrically thick and hotter, and allows efficient mixing of the Keplerian component with the sub-Keplerian one to make this region optically slim. Thus, this post-shock flow becomes an ideal site for intercepting a fraction of low-energy photons originating from the Keplerian disc and inverse-Comptonizing them to higher energies. The shock-compressed post-shock flow also allows the formation of outflow. TCAF model, as included in XSPEC (K. A. Arnaud 1996), is being extensively used to model X-ray observations from high-energy sources (D. Debnath, S. K. Chakrabarti & S. Mondal 2014; S. K. Chakrabarti, S. Mondal & D. Debnath 2015; A. A.

★ E-mail: sgarain@iiserkol.ac.in (SKG); ad21ms075@iiserkol.ac.in (AD)

Molla et al. 2017; J. R. Shang et al. 2019; P. Nandi et al. 2021; S. K. Nath et al. 2024; A. C. Eze et al. 2025).

Shock formation in the transonic accretion solution requires the presence of more than one X-type sonic point (J. Fukue 1987; S. K. Chakrabarti 1989). Subsonic flow from an infinite distance first accelerates to supersonic speed by crossing the outer X-type sonic point. This supersonic flow then undergoes a shock transition, and the post-shock flow again accelerates to supersonic speed (i.e. passes through the inner X-type sonic point) before reaching black hole horizon (satisfying inner boundary condition). Parameter space spanned by ϵ and l shows that such a condition of more than one X-type sonic point is satisfied for a limited range of these parameters (see e.g. S. K. Chakrabarti 1990; S. Das, I. Chattopadhyay & S. K. Chakrabarti 2001). Even within this limited region, the occurrence of shock in the accretion solution requires that the entropy of flow at the outer sonic point be less than that at the inner sonic point. This imposes further restrictions and makes the parameter space for the shock even more shrunk (S. Das et al. 2001). Moreover, RH analysis can locate a shock that is standing (i.e. stationary). On the other hand, multidimensional numerical simulations indicate that a shock can form in non-dissipative flow with parameters outside this allowed parameter space (D. Molteni, G. Lanzafame & S. K. Chakrabarti 1994; D. Ryu, S. K. Chakrabarti & D. Molteni 1997; D. Molteni, G. Gerardi & V. Teresi 2006; K. Giri et al. 2010; S. K. Garain & J. Kim 2023). Not only this, the shock surface can oscillate both radially as well as vertically (A. Deb, K. Giri & S. K. Chakrabarti 2016; S. K. Garain & J. Kim 2023). There are also instances of multiple shock formation inside the accretion solution. Such oscillating shocks are believed to produce quasi-periodic oscillations (QPOs) in the TCAF model (S. K. Chakrabarti et al. 2015, and references therein). However, such simulations are carried out for a few sets of parameters outside the said parameter space in isolated ways.

Several other groups independently investigated the non-dissipative sub-Keplerian accretion solutions using numerical simulations and found a variety of solutions. GR hydrodynamic simulations of J. R. Wilson (1972) and J. F. Hawley, L. L. Smarr & J. R. Wilson (1984) find shocked accretion solutions, though the shocks are unstable and move outward. D. Ryu et al. (1995) considers accretion on to a Newtonian star using a non-GR code and reports standing as well as oscillating accretion shock solution. D. Proga & M. C. Begelman (2003a, b) study the accretion of low-angular momentum flow on to a non-rotating black hole described by pseudo-Newtonian potential and find formation of a non-accreting torus close to the equator. In these simulations, infalling matter starts accreting from the outer boundary with a small, latitude-dependent l with l being highest at the equator and zero near the pole. A similar set-up is used in GR hydrodynamic simulations of P. Suková, S. Charzyński & A. Janiuk (2017) and H. R. Olivares, M. A. Mościbrodzka & O. Porth (2023). These simulations show a variety of solutions with various choices of l, and find shock and post-shock torus formation for some cases. There are non-GR and GR magnetohydrodynamic simulations also studying the flow profile, including shock of low angular momentum accretion on to black holes (S. K. Garain et al. 2020; J. Mao et al. 2025).

All the above-mentioned simulation works thus agree that for a certain range of flow parameters, shocks can form in the accretion flow. Model-based analytical works have identified the parameter space for standing shock formation. However, numerical simulations seem to indicate that various types of shock solutions (standing, propagating, oscillating, etc.) are possible. In this work, we perform a thorough investigation using multidimensional numerical simulation on a much larger parameter space than the theoretically predicted space and aim to identify the parameter space which shows shock formation in the accretion solution. To our knowledge, no such simulation-based parameter space identification for shock has been done earlier. We use the analytically calculated parameter space as our guide and perform our scan inside a rectangular region surrounding this. We choose more than 280 sets of (l, ϵ) pairs inside this rectangular region and perform a two-dimensional simulation (assuming axisymmetry) of a geometrically thick accretion disc corresponding to each set. We perform systematic analysis on this simulated accretion disc configurations to identify whether it is accretion or outflow dominated, and if it is accretion dominated, how does the shock surface behave (in case shock forms). Based on our findings, we mark a set, and finally, we draw the boundary of the parameter space for the shock in the accretion flow. We also mark the no-shock, oscillatory shock and outflow-dominated regions.

Our paper is organized as follows. In Section 2, we review the analytical method for identifying the (l, ϵ) parameter space for shock formation in the transonic, sub-Keplerian accretion flow. In Section 3, we present our multidimensional simulation procedure. In Section 4, we present our results. Finally, in Section 5, we provide a summary and our concluding remarks.

In our following calculations, we use $r_g = 2GM_{\rm bh}/c^2$ as unit of distance, r_g/c as unit of time and $r_g c$ as unit of specific (i.e. per unit mass) angular momentum. Specific energy is measured in units of c^2. Here, G is the gravitational constant, $M_{\rm bh}$ is the mass of the black hole, and c is the speed of light in vacuum.

2 ANALYTICAL METHOD FOR PARAMETER SPACE IDENTIFICATION

In this section, we briefly describe the methods to identify the parameter space for shock formation. Several works describe the parameter space calculation method for non-dissipative transonic accretion flow on to non-rotating black holes (S. K. Chakrabarti 1989; D. Molteni et al. 1994; S. Das et al. 2001; S. Mondal & S. K. Chakrabarti 2006; S. Mondal & P. Basu 2020). We use a semi-analytic method for reproducing the parameter space.

Non-dissipative flow is described by the following energy and mass conservation equations:

$$\epsilon = \frac{v_e^2}{2} + \frac{a_e^2}{\gamma - 1} + \frac{l^2}{2r^2} - \Phi, \tag{1}$$

$$\dot{M} = v_e \rho r h. \tag{2}$$

Here, r is the distance from the black hole, $v_e(r)$ is the fluid velocity on the equator, $a_e(r)$ is the sound speed at the equator, $\rho(r)$ is the density, and $h(r)$ is the disc half-thickness. $\Phi(r)$ represents the gravitational potential. For current work, we use $\Phi(r) = -1/2(r-1)$ (B. Paczyński & P. J. Wiita 1980). We perform the calculation for the vertical equilibrium model and hence, use $h(r) = a_e r^{\frac{1}{2}}(r-1)$ (S. K. Chakrabarti 1990). These equations are used along with the equation of state

$$P = K\rho^{\gamma}, \tag{3}$$

with P being the pressure, K being a constant measuring the entropy, and $\gamma = 4/3$ being the polytropic index. This equation of state provides us with

$$a_e^2 = \frac{\gamma P}{\rho} = \gamma K \rho^{(\gamma-1)}. \tag{4}$$

This equation allows to substitute ρ form equation (2) and express $\dot{M}$ in terms on v_e and a_e. Next, this equation and equation (1) are differentiated w.r.t r keeping in mind that both $\mathrm{d}\epsilon/\mathrm{d}r = 0$ and $\mathrm{d}\dot{M}/\mathrm{d}r = 0$. Now, eliminating $\mathrm{d}a_e/\mathrm{d}r$ from both equations, one can obtain

$$\frac{\mathrm{d}v_e}{\mathrm{d}r} = \frac{\frac{2a_e^2}{\gamma+1}\cdot\frac{5r-3}{2r(r-1)} - \frac{1}{2(r-1)^2} + \frac{l^2}{r^3}}{v_e - \frac{2a_e^2}{(\gamma+1)v_e}}. \tag{5}$$

One can now perform the so-called sonic (critical) point analysis on this equation. This yields

$$v_{e,c}^2 = \frac{2}{(\gamma+1)}a_{e,c}^2 \tag{6}$$

and

$$a_{e,c}^2 = \frac{(\gamma+1)(r_c-1)}{r_c^2(5r_c-3)}\left[\frac{r_c^3}{2(r_c-1)^2} - l^2\right] \tag{7}$$

at the critical point $r = r_c$. Thus, at the critical point we have

$$\epsilon = \frac{v_{e,c}^2}{2} + \frac{a_{e,c}^2}{\gamma-1} + \frac{l^2}{2r_c^2} - \frac{1}{2(r_c-1)}. \tag{8}$$

Upon using equations (6) and (7) in this equation, one obtains a quartic equation in r_c. The solution allows for locating the critical points: for a given set of l and ϵ, one can solve this equation analytically or numerically, and identify whether the given (l,ϵ) pair allows the existence of three critical points outside the black hole horizon. Out of these three critical points, the outermost and innermost points are X-type, and the middle one is O-type. If a pair satisfies this condition, we proceed to compute the solution and identify the shock location. Equation 5 can now be solved numerically using fourth-order Runge–Kutta scheme to obtain $v_e(r)$ and subsequently, $a_e(r)$ and hence the Mach number $M(r) = v_e/a_e$. Solution branches passing through both the X-type critical points are found. Next, we use the shock invariant combination of Mach numbers (following S. K. Chakrabarti 1989), which is continuous across the shock, to find the existence and location of the shock. To identify the shock formation parameter space spanned by (l,ϵ), we scan a rectangular domain $[1.4{:}2.0]\times[0.00001{:}0.0177]$ using 31×60 pairs and identify the pairs that allow shock formation. The shaded region in Fig. 1 shows the said parameter space.

Stability analysis of accretion flows involving shocks has been performed by several groups. S. K. Chakrabarti (1989) has performed a local stability analysis and demonstrated that shocks are stable in the short-wavelength limit. Several other subsequent global stability analysis (K. Nakayama 1992, 1994; K. Nobuta & T. Hanawa 1994; W.-M. Gu & T. Foglizzo 2003; W.-M. Gu & J.-F. Lu 2006) demonstrate that these shock structure may be stable under various conditions. Two-dimensional, time-dependent numerical simulations of shocked accretion flows in the equatorial plane with non-axisymmetric azimuthal perturbations reveal that axisymmetric shock structure becomes non-axisymmetric (D. Molteni, G. Tóth & O. A. Kuznetsov 1999). However, this non-axisymmetric, spiral shock structure is stable. Such simulations are extended to three-dimensions in S. K. Garain & J. Kim (2023) where we again confirm the same conclusion.

3 SIMULATION PROCEDURE

For this study, we run more than 280 number of two-dimensional ideal hydrodynamics simulations in the $R-Z$ cylindrical domain. We assume axisymmetry in the ϕ direction. The following

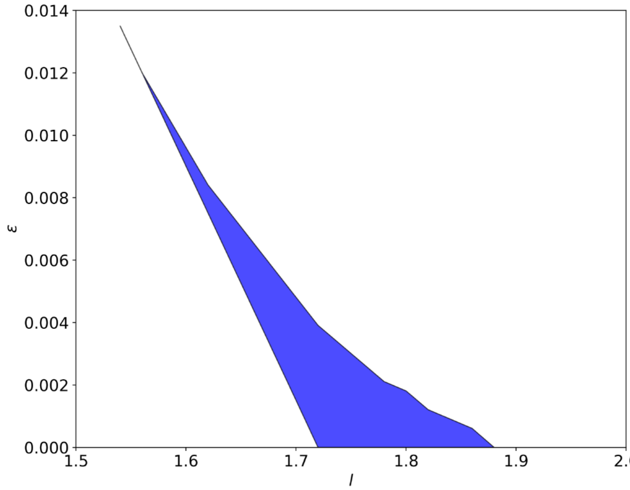

Figure 1. Shows allowed parameter space in the $l-\epsilon$ plane for the standing shock formation in the non-dissipative sub-Keplerian accretion flow. This is found using analytical method.

conservation equations are solved numerically:

$$\frac{\partial\mathbf{U}}{\partial t} + \frac{1}{R}\frac{\partial(R\mathbf{F_R})}{\partial R} + \frac{\partial\mathbf{F_Z}}{\partial Z} = \mathbf{S}, \tag{9}$$

where the vector of conserved variables $\mathbf{U}$, R-flux $\mathbf{F_R}$, and Z-flux $\mathbf{F_Z}$ can be written as

$$\mathbf{U} = \begin{pmatrix}\rho\\ \rho v_R\\ \rho l\\ \rho v_Z\\ E\end{pmatrix};\quad \mathbf{F_R} = \begin{pmatrix}\rho v_R\\ \rho v_R^2 + P\\ \rho l v_R\\ \rho v_R v_Z\\ (E+P)v_R\end{pmatrix};\quad \mathbf{F_Z} = \begin{pmatrix}\rho v_Z\\ \rho v_R v_Z\\ \rho l v_Z\\ \rho v_Z^2 + P\\ (E+P)v_Z\end{pmatrix}$$

And the source term is

$$\mathbf{S} = \begin{pmatrix}0\\ \frac{\rho v_\phi^2}{R} + \frac{P}{R} - \rho\frac{\partial\Phi}{\partial r}\frac{R}{r}\\ 0\\ -\rho\frac{\partial\Phi}{\partial r}\frac{Z}{r}\\ -\rho\frac{\partial\Phi}{\partial r}\frac{(Rv_R+Zv_Z)}{r}\end{pmatrix}.$$

Here, ρ is density, v_R, v_ϕ, v_Z are three components of velocity, P is pressure, $E = \frac{1}{2}\rho(v_R^2+v_\phi^2+v_Z^2) + \frac{P}{\gamma-1}$ and $l = Rv_\phi$. r represents the spherical radius and is given by $r = \sqrt{R^2+Z^2}$. $\Phi(r) = -1/2(r-1)$ represents the gravitational potential. We use polytropic equation of state $P = K\rho^\gamma$ with $\gamma = 4/3$ and K being a measure of entropy. The vector of primitive variables is denoted by

$$\mathbf{V} = \begin{pmatrix}\rho\\ v_R\\ v_\phi\\ v_Z\\ P\end{pmatrix}.$$

We use similar simulation set up which has been used over decades to simulate such transonic accretion flow (S. K. Chakrabarti & D. Molteni 1993b; D. Ryu et al. 1995; D. Molteni et al. 1996; S. K. Chakrabarti, K. Acharyya & D. Molteni 2004; T. Okuda, V. Teresi & D. Molteni 2007; K. Giri et al. 2010; S. K. Garain, H. Ghosh & S. K. Chakrabarti 2012; T. Okuda & D. Molteni 2012; S. Das et al. 2014; S. K. Garain, H. Ghosh & S. K. Chakrabarti 2014; S.-J. Lee et al. 2016; J. Kim et al. 2017, 2019;

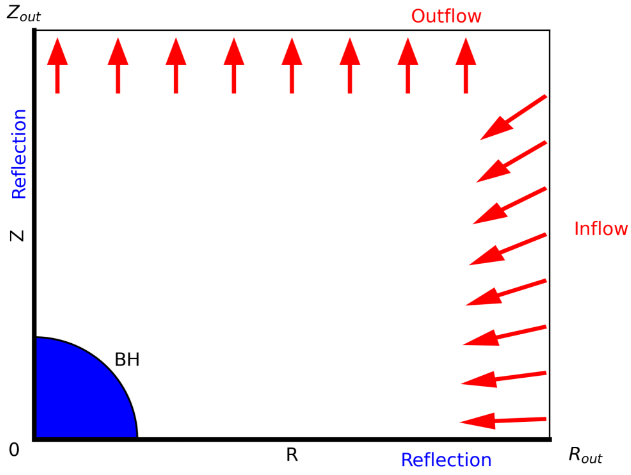

Figure 2. Shows the simulation domain and the set up. Inflow boundary condition is used at $R = R_{\rm out}$ and outflow boundary condition is used at $Z = Z_{\rm out}$. Matter is absorbed inside $r = r_{\rm BH}$ (blue region). Reflection boundary conditions are used on the axis ($R = 0$) and the equator ($Z = 0$).

S. K. Garain & J. Kim 2023; S. Debnath et al. 2024). Our simulation set-up is sketched in Fig. 2. The simulation domain is $[0 : R_{\rm out}]$x$[0 : Z_{\rm out}]$. A black hole with radius $r_{\rm BH} = \sqrt{R^2 + Z^2} = 1.8$ is placed at the origin. To mimic matter absorption by the black hole, we set ρ and P to respective floor values and the velocity components to zero on all grid points inside $r = r_{\rm BH}$. We allow matter coming from far away to enter our simulation domain through the outer radial boundary. Thus, we impose an inflow boundary condition at $R = R_{\rm out}$, i.e. we maintain a constant **V** on the ghost zones of this boundary. The disc half-height at injection is assumed to be $h = Z_{\rm out} = R_{\rm out}/2$. Reflection boundary condition is used on the axis $R = 0$ and on the equator $Z = 0$. Because our flow is axisymmetric, the velocity components normal to the rotation axis cancel out. This justifies reflection boundary condition on the axis. For our flow, matter rarely reaches $R = 0$ because of non-zero angular momentum. Hence, the flow profile is generally insensitive to this specific boundary condition, which is verified for a few cases. Reflection boundary condition on the equator $Z = 0$ arises due the assumption that the flow dynamics is symmetric with respect to the equator. Thus, the velocity components normal to the equator is exactly zero at $Z = 0$ leading to zero mass flux across the equator. This assumption imposes some restriction though as discussed in Section 5. The outflow boundary condition is used on the upper Z-boundary $Z = Z_{\rm out}$. The simulation domain is initially filled with static background matter having density and pressure as respective floor values.

Our numerical solution scheme is the same as in S. K. Garain & J. Kim (2023). We use the finite volume method, and the code is globally second-order accurate. The spatial reconstruction is done using the van Leer limiter, interfacial fluxes are calculated using the HLL Riemann solver, and the time-integration is done using a two-stage strong stability preserving Runge–Kutta scheme.

Since the numerical solutions depend on the inflow boundary condition, we describe its implementation in details here. The inflow parameters **V** need to be found at all radial and vertical ghost zones adjacent to the outer radial boundary at $R = R_{\rm out}$. In the radial direction, we use two ghost zones, and we use the same **V** in both. However, **V** varies in the vertical direction. We first compute **V** at the equator. v_e and a_e are computed following Section 2 for a given (l, ϵ) pair. We set $v_R = v_e$ and $v_Z = 0$. Since the simulations are non-dissipative, density $\rho = \rho_e$ is scaled to 1. This allows us to compute pressure $P = P_e = a_e^2\rho_e/\gamma$. l value allows to calculate $v_\phi = l/R_{\rm out}$. Once **V** at the equator is set, we proceed to compute its values at other heights. Note that if we use the equatorial **V** at different heights, resulting ϵ will not remain constant due to reducing gravitational energy $\frac{1}{2(r-1)}$ with heights. To compensate for this, we reduce $v_r = \sqrt{(v_R^2 + v_Z^2)}$ and a with increasing height such that the v_r/a ratio remains the same as the equatorial Mach number v_e/a_e. This ensures that the injected flow has a constant ϵ. v_R and v_Z are chosen in a way that v_r vector points to the central black hole. Next, we enforce the flow to be isentropic at all heights. This allows us to find the density ρ at all heights using $\rho = \left(\frac{a^2}{\gamma K_e}\right)^{1/(\gamma-1)}$, with K_e being the equatorial entropy $K_e = P_e/\rho_e^\gamma$. Using this ρ, $P = K_e\rho^\gamma$ is found at all heights. v_ϕ is computed using $v_\phi = l/R_{\rm out}$.

4 RESULTS

Using the above numerical simulation scheme and boundary conditions, we aim to find a parameter space analogous to the one shown in Fig. 1. For this, we scan the (l, ϵ) domain [1.4:1.9] $\times$ [0.0001:0.0061] using judiciously chosen 286 points (each point corresponds to a (l, ϵ) pair). The outermost X-type critical radius (r_c) is calculated for a given point, and it is used to determine the simulation domain. $R_{\rm out}$ is chosen to be just inside this r_c and $Z_{\rm out} = R_{\rm out}/2$. Thus, we don't simulate a flow passing through the outer sonic point. Rather, matter starts with a supersonic speed from the outer boundary. This supersonic injection ensures that the inflow properties remain unaffected from the acoustic feedback from the interior of the simulation domain and correctly represent the flow solution corresponding to given conserved inflow parameters. This practice is followed in all the references mentioned above. Clearly, our simulation domains vary with the points. We adjust number of grids in the R and the Z directions accordingly. For the chosen range of parameters, the outermost r_c ranges between 34.4 and 2995.4. Thus, the lowest value of $R_{\rm out}$ across our simulations is 29. However, due to limited computational resources, the highest value of $R_{\rm out}$ across our simulations is restricted to 250. For all simulations, we use ratioed grids in the R and Z with a common ratio of 1.003. Before fixing the grid numbers, we experimented with a few cases and confirmed that the final solution doesn't depend on the grid size (i.e. solution is converged.) All simulations have been run till $t = 50\,000$.

4.1 Parameter space

We run the multidimensional simulation for each point of the parameter space and confirm that it reaches a steady state by simulation stopping time. During the run, we compute the shock location on the equatorial plane $Z = 0$. This time-series data allows us to identify whether a shock is formed for this point, and if yes, whether it is standing or time varying. This way, we categorize all 286 points based on the solution characteristics and identify a bulk region on the (l, ϵ) plane that shows shock formation. Area inside the red-dashed curve in Fig. 3(a) represents this region. The analytically determined parameter space for the standing shock is also shown here by the black solid line. Note that, unlike the smooth boundary found using the analytical method, the numerically identified boundary is slightly jagged. This is the manifestation of scanning the (l, ϵ) domain with finite number

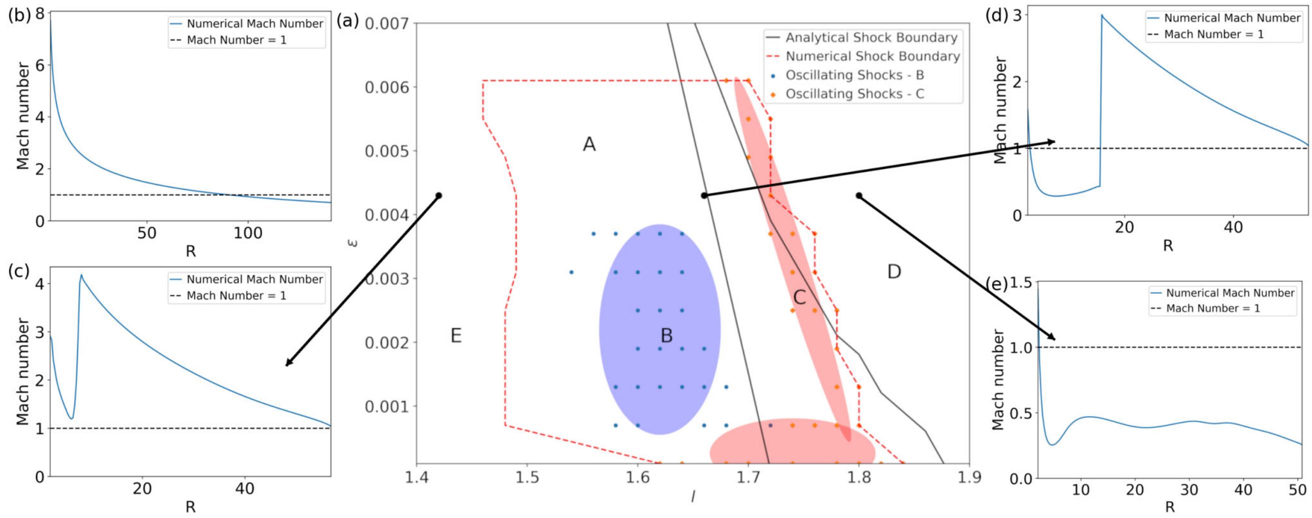

Figure 3. Classification of parameter space for the non-dissipative sub-Keplerian accretion flow using numerical simulation. The red dashed line in (a) surrounds the parameters which show shock formation. The solid black lines overplot the boundary of the shaded region shown in Fig. 1. Shocks can be standing or oscillatory. Region marked **A** shows standing shock solutions. Numerical simulations identify different types of oscillatory shocks in regions marked **B** (blue) and **C** (pink). Parameters from region **E** do not show shock formation though the effect of centrifugal barrier may be present. Accretion flow with parameters from region **D** passes through inner sonic point only. Four plots surrounding (a) demonstrate the gradual change in the solution nature with increasing l for a given $\epsilon = 0.0043$ value. Radial Mach number variation along the equator is plotted in these plots. (b) shows the standard Bondi solution profile for $l = 0$. With increasing l, the centrifugal barrier becomes prominent. (c) shows the solution with the barrier but without a shock for $l = 1.42$. (d) shows the solution with a shock for $l = 1.66$. Finally, with much higher $l = 1.8$, the solution shows presence of only the inner sonic point.

of points. One may find smoother boundary by increasing the number of scanning points.

We identify this shock parameter space boundary curve at the lower and upper l values by analysing the gradual change of the solution nature. Four plots surrounding Fig. 3(a) demonstrates this gradual change in the solution nature because of increasing l for a given $\epsilon = 0.0043$ value. Radial Mach number variation along the equator is plotted in these plots. For a given value of ϵ, the solution corresponding to the lowermost l value (i.e. $l = 0$) is the standard Bondi accretion solution having only one sonic point: a subsonic flow far away from the black hole becomes supersonic after crossing this sonic point. Fig. 3(b) shows such solution for $\epsilon = 0.0043$, $l = 0$. For points just outside the left red-dashed line boundary, the equatorial Mach number profiles show clear evidence of slow down due to centrifugal barrier, but the flow remains supersonic. This ensures absence of inner sonic point for such parameters. Fig. 3(c) shows such a solution for $\epsilon = 0.0043$, $l = 1.42$. This region is marked as **E**. For slightly higher l, the equatorial Mach profiles show steady supersonic to subsonic transition (shock solution) and subsequently accreting flows pass through the inner sonic point before getting accreted supersonically. Fig. 3(d) shows such a solution for $\epsilon = 0.0043$, $l = 1.66$. For some cases, the shock solutions are oscillatory. Region **A** shows the points with steady shock solutions, whereas, regions **B** and **C** show the oscillatory shock solutions. With increasing l (larger centrifugal barrier), the shock moves away from the black hole. And finally, we find a situation when the shock reaches the outer boundary of the domain leaving behind the subsonic flow which passes through the inner sonic point before getting accreted supersonically. Fig. 3(e) shows such a solution for $\epsilon = 0.0043$, $l = 1.8$. Points from region **D** (right to the upper l boundary) show these solutions. We discuss examples of solutions from each of these regions separately below.

We observe that the simulation-based parameter space for shock is larger, specifically for lower l, than the analytical calculation-based parameter space. In analytical calculations, the flow is assumed to be in vertical equilibrium i.e. vertical pressure gradient force is balanced by the vertical component of gravity. This balance does not allow vertical motion of the fluid as the net force in the vertical direction is zero. In contrast, we find significant amount of vertical motion in our simulations, specifically just after the flow passes the centrifugal barrier. This vertical motion accumulates a large part of the inflowing matter closer to the equatorial region, thereby enhance the pressure in the equatorial region, which helps in shock formation. For example, a set of parameters, $\epsilon = 0.0055$ and $l = 1.66$, allows a shock formation at $r = 12.14$ as per analytical method and the density compression is found to be 2.11. However, the numerical simulations detects a steady shock at $R = 16.06$ on the equator with a density compression of 3.7. This extra compression results in extra pressure build up in the post-shock region. One may add this extra pressure term parametrically in the Rankine-Hugoniot analysis to analytically find the shock location as done in D. Molteni et al. (1994) and demonstrate that shock actually forms farther for a reasonable value of the parameter. For this case, the parameter value is found to be 0.1 which is reasonable (see D. Molteni et al. (1994)). This same reason allows formation of shock in numerical simulations for the parameter sets with lower l values, which do not accept shock solution analytically.

In passing, we also wish to mention that in full three-dimensional (3D) simulation, flow is dynamically active in all three spatial directions. However, if a full axisymmetric inflow boundary condition is imposed, the flow remains axisymmetric throughout the domain because the centrifugal barrier is axially symmetric and fluid parcels along all ϕ are affected in the same manner. This is demonstrated in S. K. Garain & J. Kim (2023).

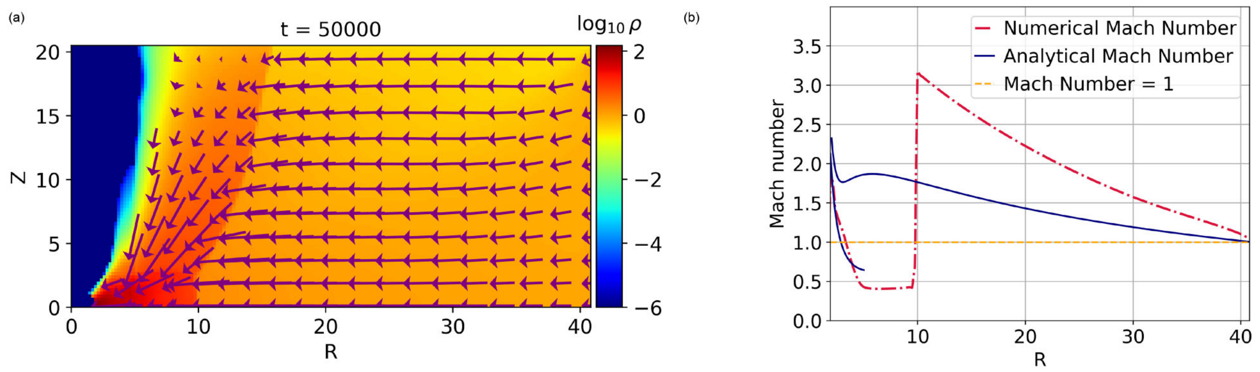

Figure 4. (a) $\log_{10}\rho$ distribution with velocity vectors overplotted and (b) radial variation of Mach number are shown here for a typical point of **A** region in Fig. 3(a). This is an example of standing shock solution in our simulation. Parameters $\epsilon = 0.0055$ and $l = 1.62$ are used for this simulation. This set of parameters does not allow shock formation as per analytical method. However, numerical simulation shows standing shock formation at $R = 9.98$ on the equator.

Since the flow remains fully axisymmetric, there is no difference between our current 2D and a similar 3D flow structure. So we believe that the shock parameter space found in this work will remain the same if we repeat the task using 3D simulation with full axisymmetric inflow boundary condition. However, if non-axisymmetric variation (through e.g. a density perturbation) is explicitly introduced in the ϕ direction of a 3D simulation, flow develops non-axisymmetric structure and solution profiles differ significantly from a 2D flow structure. In several works (D. Molteni et al. 1999; H. Nagakura & S. Yamada 2008, 2009; S. K. Garain & J. Kim 2023), it is reported that such a perturbed flow develop larger post-shock, turbulent region. Thus, it is possible that the shock parameter space may change in 3D simulations with non-axisymmetric structure.

4.1.1 Region **A**

Our numerical simulations find solutions with standing as well as oscillatory shocks. For a significant part of the scanned space, shocks are non-oscillatory or oscillatory with a very small amplitude ($< 2r_g$). We mark that region of space with **A** in Fig. 3(a). Typical solution profile for a point in this region is shown in Fig. 4. $\epsilon = 0.0055$ and $l = 1.62$ are used for this case. This simulation has been conducted in a simulation domain [0:40.82]×[0:20.34] using [148 × 74] ratioed grids. Fig. 4(a) shows the $\log_{10}\rho$ distribution in colour, overplotted with velocity vectors. The solution at time $t = 50\,000$ is shown here. One can identify the parabolic shock surface from the density contrast starting at the equator around $R = 10$ and moving vertically up. This surface is known as centrifugal barrier supported boundary layer (CENBOL). Fig. 4(b) shows the radial variation of the Mach number along the equator (dash–dotted line), and the shock location is $R = 9.98$ on the equator. We additionally plot the Mach number profile obtained from the analytical method (solid line). Branches passing through the outer and the inner sonic points are shown. However, the analytical solution is shock free. The numerical solution shows shock solution and post-shock flow follows the analytical branch passing through the inner sonic point. For all the other points in this region, the solution profile is mostly similar except that the shock is located nearer or farther from the black hole. We find that for a given ϵ, the shock location moves farther out with increasing l. On the other hand, for a given l, the shock location moves farther out with increasing ϵ.

4.1.2 Region **E**

Solution profile for a typical point in region **E** also shows the presence of CENBOL, albeit in a very weak form. This is understandable because a lower l would produce a weaker centrifugal barrier. Fig. 5(a) shows the $\log_{10}\rho$ distribution in color, and (b) shows the Mach number profile along the equator (dashed-dot line) for a typical point from this region. Here again, we show the Mach number profile obtained from the analytical method (solid line). Only outer sonic point exists for this case. $\epsilon = 0.0019$ and $l = 1.46$ are used for this case. The solution at time $t = 50\,000$ is shown here. This simulation has been conducted in a simulation domain [0:99.72]×[0:49.765] using [256×128] ratioed grids. We notice a very thin layer of enhanced density behind CENBOL. The Mach number profile also shows a jump. However, the flow remains supersonic even after that and accretes on to the black hole supersonically. Thus, no shock (supersonic to subsonic transition) forms for such cases and hence, the inner sonic point is also not present.

4.1.3 Region **B** and **C**

Parameters from regions marked **B** and **C** show numerical solutions with the oscillatory shocks. In Fig. 3(a), we have marked only those oscillating cases that have a significant amplitude, greater than or equal to 2. However, the nature of the oscillations is different for these two regions. We extensively discuss these solutions now.

Fig. 6 shows the time variation of shock location on the equatorial plane for two different cases, one from region marked **B** and another from **C**. The representative case from **B** has $\epsilon = 0.0013$ and $l = 1.58$. This simulation has been conducted in a simulation domain [0:99.72]×[0:49.765] using [256×128] ratioed grids. All points from this region show a similar type of higher frequency, regular oscillations. Upon careful observation, we notice that the shock oscillations are mostly confined within a region close to the equator. The upper part of the CENBOL doesn't participate in the oscillation. To demonstrate this, we plot the density distribution at four successive time points, indicated by four black solid dots within a single oscillation. The four snapshots are shown in Figs 7 (a)–(d), and they are drawn at instances $t = 24\,650$, $24\,800$, $24\,950$, $25\,100$, respectively. Colour shows $\log_{10}\rho$ distribution and arrows show velocity vectors. (a) shows that a parabolic shock surface

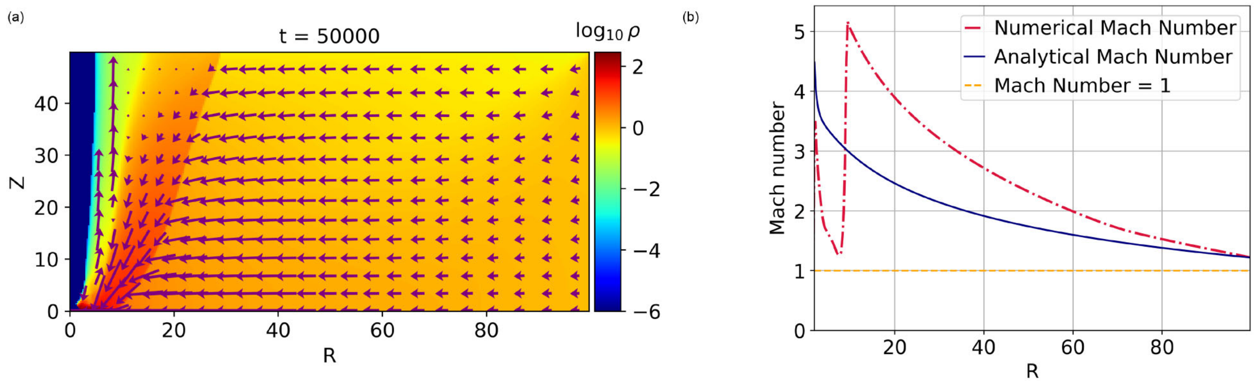

Figure 5. (a) $\log_{10}\rho$ distribution with velocity vectors overplotted and (b) radial variation of Mach number are shown here for a typical point of **E** region in Fig. 3(a). This is an example of no shock solution. Parameters $\epsilon = 0.0019$ and $l = 1.46$ are used for this simulation. This set of parameters does not show shock formation both analytically and numerically. However, numerical simulation shows piling up of matter and resulting supersonic to supersonic jump due to centrifugal barrier.

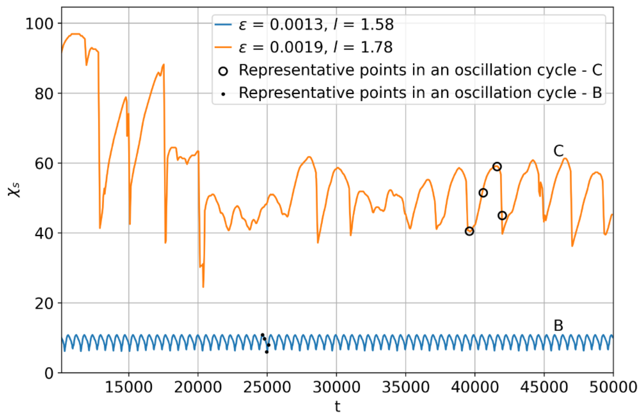

Figure 6. Time variation of shock location at the equator for two cases, one from region marked **B** and another from **C**. Flow parameters are marked in the legend. Solutions exhibit steady oscillation for both the cases. Four points in a single oscillation are marked on each plot. We show the solution profiles at these four points in subsequent figures .

touches the equator at $R = 10.8$. At subsequent times (i.e, (b) and (c)), the lower part of the shock surface moves inward ($R = 9.7$ and $R = 5.8$ respectively), and then in (d), it again starts moving outward ($R = 8.02$). During this full oscillation, the upper part doesn't move at all.

In contrast to **B**, solution for points from region **C** shows large amplitude shock oscillation as indicated by the orange line in Fig. 6. For this particular case, $\epsilon = 0.0019$ and $l = 1.78$. This simulation has been conducted in a simulation domain $[0{:}99.72]\times[0{:}49.765]$ using $[256\times128]$ ratioed grids. The solution shows oscillation of the entire shock surface. We show the density distribution at four successive time points, indicated by four black circles within a single oscillation. The four snapshots are shown in Figs 8 (a)–(d), and they are drawn at instances $t = 39\,600$, $40\,600$, $41\,600$, $42\,000$, respectively. Here, again, color shows $\log_{10}\rho$ distribution and arrows show velocity vectors. (a) shows the shock surface touches the equator around $R = 40$. We also observe the presence of a centrifugal barrier resulting in a sudden density increase around $r = 50$. However, this is not a shock as the flow is still supersonic. The shock location subsequently moves outward to nearly $R = 60$ in (c). At the end of the oscillation, it comes back to around $R = 40$ in (d). As one can see, a large portion of the disc participates in the shock oscillations. We observe the presence of large turbulent vortices in the solution for points from region **C**.

4.1.4 *Region* ***D***

The area to the right of the shock-forming boundary, marked by **D** in Fig. 3(a), represents outflow-dominated, nearly non-accreting solutions. A representative example of solution is shown in Fig. 9. $\epsilon = 0.0043$ and $l = 1.8$ are chosen for this one. This simulation has been conducted in a simulation domain $[0{:}50.78]\times[0{:}25.308]$ using $[148\times74]$ ratioed grids. In Fig. 9(a), we show $\log_{10}\rho$ distribution in color, and arrows show velocity vectors. The snapshot is drawn at time $t = 50\,000$. The radial variation of Mach number along the equator for this case is shown in Fig. 9(b). This plot shows that the flow is subsonic at all radii except at the injection point and becomes supersonic only before getting accreted. The successive snapshots shows that these flows develop an outward propagating shock which reaches the outer boundary of the domain, leaving behind the subsonic flow. A significant amount of injected matter can be seen to leave as outflow and form a vortex-like structure, causing nearly no accretion of matter on to the black hole. For higher l flows, the centrifugal barrier is sufficiently strong to stop matter from getting accreted. Prior numerical simulations in J. Kim et al. (2019) also reported a similar flow profile for higher l (see Fig. 7 of this paper).

4.2 Parameter dependence of shock location

The location and behaviour of the shock surface vary with the flow parameters. We have extracted the parameter dependence of the shock location from the simulated data. In Fig. 10, we plot the shock-location χ_s along the vertical axis and ϵ along the horizontal axis. Each line on this plot shows the variation of shock location for a fixed l value (marked on the plot). The inset shows a zoomed-in part of overlapping region. Note that this plot is done using only the points from region **A** of Fig. 3(a) since we find the presence of a shock for these parameters. Also note that in many cases, the shock surface is time-dependent. Therefore, we show the time-averaged value of the shock location at the equator in this plot. This plot demonstrates that for a given value of ϵ, the shock location generally increases with l. For a fixed value of l, the variation of the shock location w.r.t. ϵ is not monotonic though.

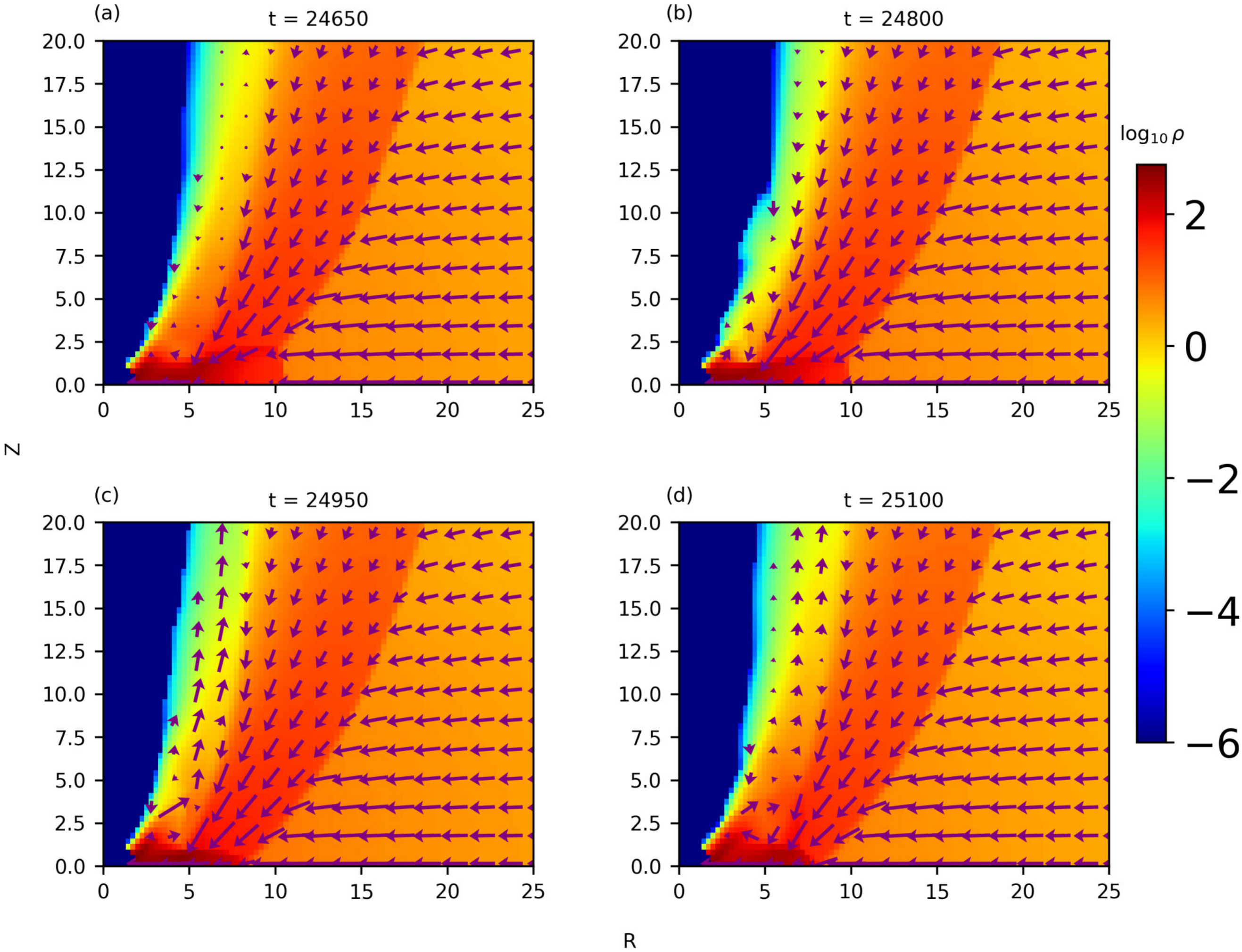

Figure 7. $\log_{10}\rho$ (colour)—velocity vector snapshots at $t = 24\,650$ (a), 24 800 (b), 24 950 (c), and 25 100 (d) revealing the accretion disc dynamics over a full oscillation for a set of parameters from region **B**. These timestamps are marked by four solid black points in Fig. 6. Simulation parameters $\epsilon = 0.0013$ and $l = 1.58$ are used for this simulation. See the text for details.

For some part, we observe the shock location increases with ϵ, but we also observe that the shock location either does not change much or slightly decreases with increasing ϵ (especially for lower l values).

4.3 Parameter dependence of outflow

In almost all our simulations, we observe the formation of outflow. The outflow originates due to the combined effects of centrifugal barrier and thermal pressure gradient force. In Appendix A, we perform a force analysis to demonstrate this. To quantify the outflow, we compute the outgoing mass flux $\dot{M}_{\rm out}$ through the upper Z boundary. We also compute the mass absorption rate $\dot{M}_{\rm abs}$ by the black hole sitting inside $r = r_{\rm BH}$. We generally observe that for points in region **A** and **E**, the solutions are absorption dominated, i.e. most of the injected matter inside the simulation domain is accreted by the black hole. However, as we move more towards the higher l region (i.e. region **D**), the solution becomes outflow dominated.

In Fig. 11, we show three examples of outflow and absorption rates. The plots show time variation of the ratio $\dot{M}_{\rm out}/\dot{M}_{\rm in}$ (orange line) and $\dot{M}_{\rm abs}/\dot{M}_{\rm in}$ (blue line), where, $\dot{M}_{in}$ is the inflowing mass flux through the outer R boundary. Fig. 11(a) shows these ratios for the point from region **A**. We find that on average, nearly 95.45 per cent of the injected matter is getting accreted in this case. Fig. 11(b) shows the same as (a) for the point from region **E**. For this case, we also find that nearly 95.66 per cent of matter is getting accreted. Fig. 11(c) shows the ratios for the point from region **D**. For this case, the solution shows the formation of large vortices, which are primarily caused by the interaction between the incoming matter and the bounced-back matter from the centrifugal barrier. Because of this strong centrifugal barrier, matter cannot get accreted on to the black hole and mostly leaves the system as outflow. We observe that more than 86 per cent matter leaves the domain as outflow.

5 SUMMARY AND DISCUSSIONS

In this paper, we numerically simulate the non-dissipative, sub-Keplerian accretion flow on to a non-rotating black hole for a range of flow parameters spanned by specific energy ϵ and specific angular momentum l. Such accretion solutions are known to harbour shock and produce a boundary layer (CENBOL) around a black hole for certain ranges of these parameters. The

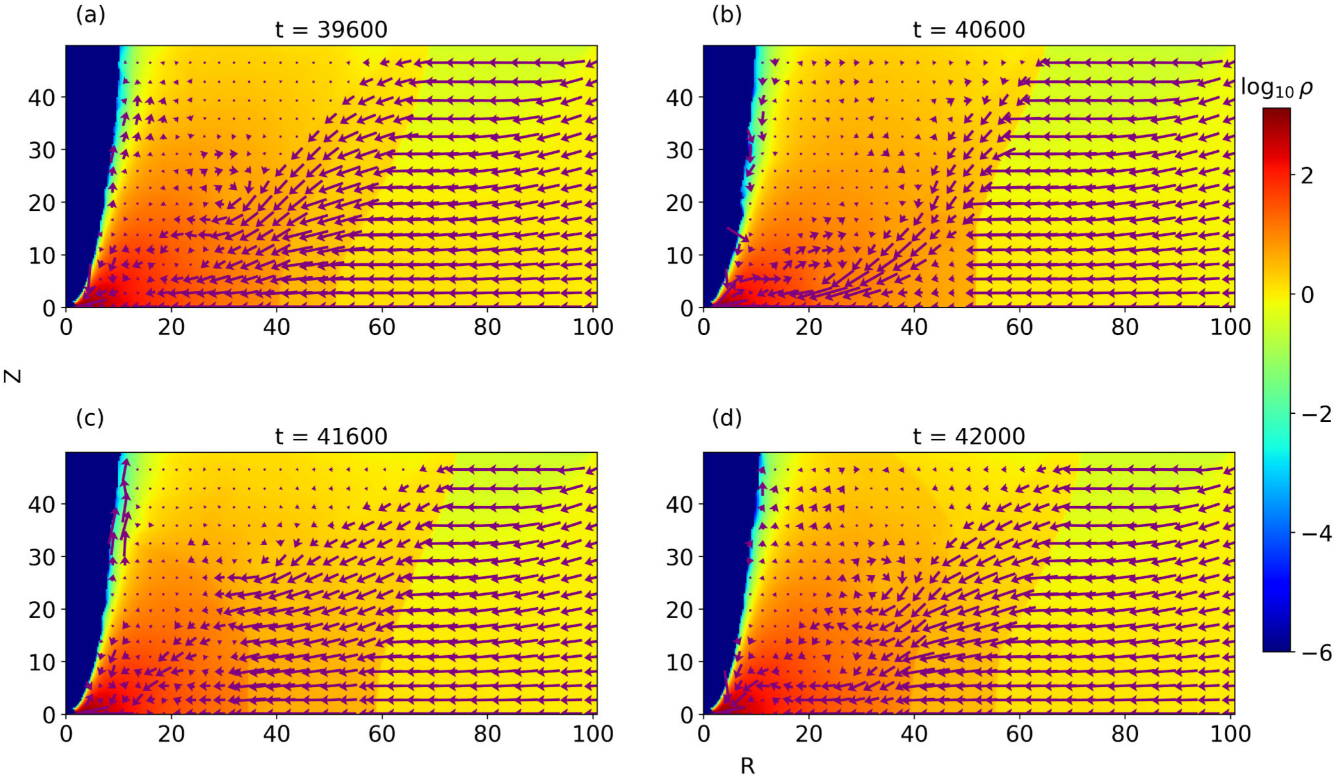

Figure 8. $\log_{10}\rho$ (colour)—velocity vector snapshots at $t = 39\,600$ (a), 40 600 (b), 41 600 (c), and 42 000 (d) revealing the accretion disc dynamics over a full oscillation for a set of parameters from region **C**. These timestamps are marked by four circles in Fig. 6. Simulation parameters $\epsilon = 0.0019$ and $l = 1.78$ are used for this simulation. See the text for details.

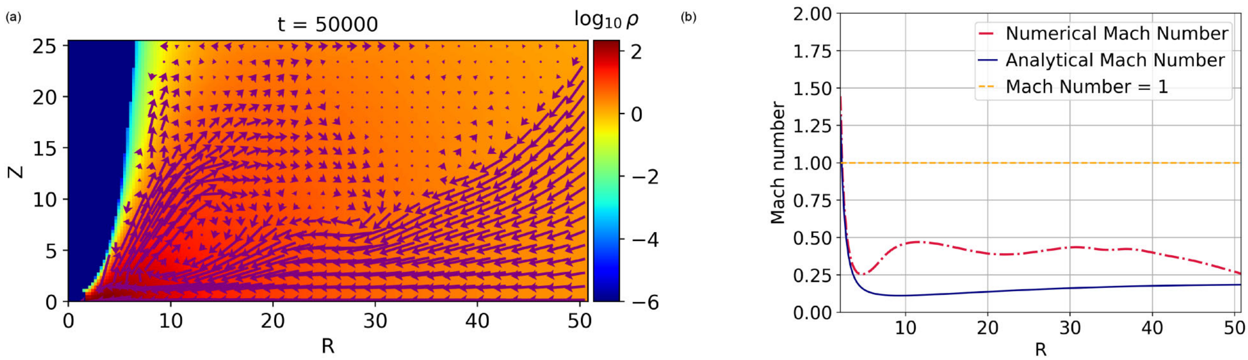

Figure 9. (a) $\log_{10}\rho$ overplotted with velocity vectors for a typical point of **D** region. This is an example of outflow-dominated, nearly non-accreting solution. (b) Radial variation of Mach number for the corresponding case. Parameters $\epsilon = 0.0043$ and $l = 1.8$ are used for this simulation. Analytically, the solution branches passing through the outer sonic point does not reach the black hole horizon for this set of parameters. Only solution branches passing through the inner sonic point reach the horizon. Numerical simulation also demonstrates that the accreting matter passes through the same inner sonic point.

theoretical method for shock parameter space identification is based on whether a solution contains a standing shock or not (S. K. Chakrabarti 1989; D. Molteni et al. 1994; S. Das et al. 2001; S. Mondal & S. K. Chakrabarti 2006; S. Mondal & P. Basu 2020). However, there are several numerical simulations that demonstrate that in multidimensional simulations, shocks can be standing or oscillatory and it can form for flow parameters even outside these theoretical limits. However, a full parameter space investigation based on purely multidimensional numerical simulations are still missing. Our current paper fills that gap.

We scan the parameter space spanned by l and ϵ in the domain [1.4:1.9] x [0.0001:0.0061] using judiciously chosen 286 points. Based on the simulation results, we identify extended ranges of these parameters that allow shock formation (Fig. 3a). Within this shock-forming region, not all points show a standing shock. There are regions that show oscillating shocks. In our analysis, we categorized a solution as oscillatory only if the oscillation amplitude is larger than $2r_g$. We broadly identify two types of oscillations. In one type (region marked **B**), only the lower part (closer to the equator) of the shock surface participates in the oscillation, the oscillation frequency is higher, and the amplitude

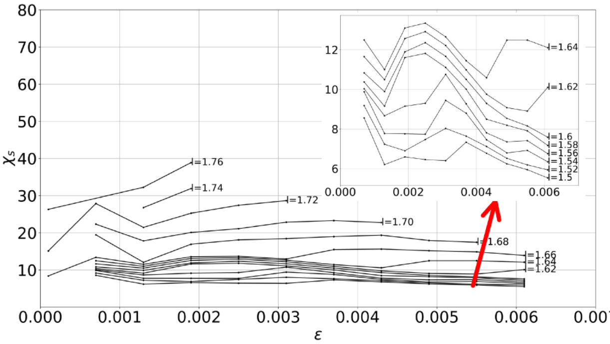

Figure 10. Variation of time-averaged shock location at the equator with ϵ for fixed l values, marked on each curve. The inset shows a zoomed-in part of the overlapping region. We find that the shock location generally increases with l for a given ϵ. However, for a fixed value of l, the variation of the shock location w.r.t. ϵ is not monotonic.

is usually smaller. In the other type (region marked **C**), the entire shock surface moves, the oscillation frequency is lower, and the amplitude is usually larger. Oscillations identified in region **B** were indicated in the theoretical analysis of S. Das et al. (2001). Additionally, similar types of oscillations as in **C** are also reported in earlier simulations (K. Giri et al. 2010). These oscillating shocks have great implications in explaining timing features such as QPOs.

From our simulation, we also extract the global parameter dependence of shock location and outflow properties. We generally find that the shock forms farther with increasing l for a given ϵ. However, variation of shock location with ϵ for a given l is found to show weak dependence. Most of our simulations naturally produce outflow due to the combined effects of centrifugal and thermal pressure gradient forces. The outflow rate depends strongly on l. All these findings generally match the previous theoretical analyses or the simulations.

Formation of a hotter, optically slim (optical depth ~ 1) disc as a result of shock in the sub-Keplerian flow, naturally explains the origin of corona around a black hole. This corona can inverse-Comptonize low-energy seed photons, originating from a truncated Shakura–Sunyaev type thin disc (N. I. Shakura & R. A. Sunyaev 1973), and produce a high-energy tail observed in spectrally hard states. In case when thin disc is absent, this corona can produce high-energy seed photons and self-Comptonize them to give rise to hard spectral states. This corona also produces outflow self-consistently which is frequently observed in a spectrally hard state. Our analysis demonstrates that a large parameter space actually exhibits such corona formation. Hence, this process may be very common in a X-ray binary system or an active galactic nuclei observed in spectrally hard state. Our simulations also reveal that certain region of parameters exhibit dynamic, oscillatory corona. Such corona will induce the oscillation in the outgoing radiation and may explain observed QPOs in the high energy band.

In passing, we note a limitation of our main result. In this work, we simulate flow profile only in the upper half of the $R-Z$ domain and use reflection symmetry along the equator. Prior experience shows that unless flow has sufficiently large l, flow profiles in both haves are similar. However, for a large value of l, the CENBOL may show vertical oscillations due to strong post-shock turbulence (A. Deb et al. 2016; S. K. Garain & J. Kim 2023) in addition to radial oscillations. In our case, large l simulations are anyway mostly classified as oscillating or outflow-dominated solutions. Thus, we believe that the parameter space boundary for shock won't be affected too much because of our use of reflection symmetry along the equator.

The exercise presented here is done for non-rotating black holes using pseudo-Newtonian potential. Similar parameter space classification around rotating black holes using fully GR calculations is also done in a few literatures (S. K. Chakrabarti 1996a, b). As shown in these references, for corotating flows, one can find shocks very close to a black hole. If such shocks oscillate with high enough frequency, they may be able to explain high-frequency QPOs found in a few sources. We shall perform parameter space investigation around rotating black holes in the future using multidimensional GR hydrodynamics simulations (S. K. Garain 2025) and the results will be reported elsewhere. Similar parameter space investigation can also be done using pseudo-Newtonian potential representation for Kerr black holes as well (S. K. Chakrabarti & R. Khanna 1992; B. Mukhopadhyay 2002; S. K. Chakrabarti & S. Mondal 2006; I. K. Dihingia et al. 2018) just by replacing the potential $\Phi(r)$ in this work. However, all these potentials have their own limitations as discussed in these references and one has to be careful about those. Full GR calculations are free from these limitations.

Finally, we recognize that our equations and hence the results are valid for ideal flow. More realistic flow may have various dissipations such as viscous transport or radiative loss. Also, magnetic field, being very pervasive, is expected to be present in the accretion flow. Inclusion of these physical components would affect the flow solutions. Hence, the parameter space may change in presence of these. However, in absence of reliable quantitative measurement of these dissipative processes, we generally rely on parametric representation of these affects. Thus, the classification of accretion solutions should also depend on the choice of these new parameters.

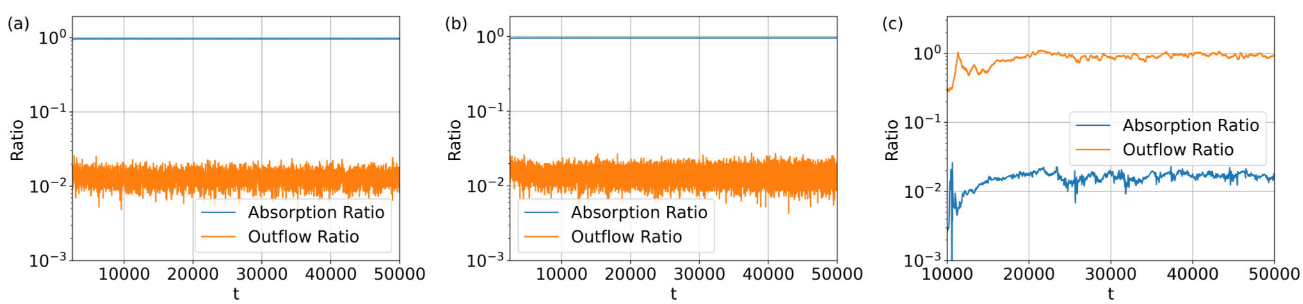

Figure 11. Time variation of mass outflow rate (orange line) and mass absorption rate (blue line), normalized by the mass injection rate into the simulation domain, for three different points in the parameter space: (a) for a point in region **A**, (b) for **E**, and (c) for **D**.

ACKNOWLEDGEMENTS

We acknowledge the usage of the Kepler Computing facility, maintained by the Department of Physical Sciences, IISER Kolkata. We also acknowledge the usage of IUCAA's Pegasus Computing facility for conducting a few simulations. SKG also acknowledges partial financial support from Anusandhan National Research Foundation through grant no. ANRF/ARGM/2025/002001/TS.

DATA AVAILABILITY

The simulation data will be available from the corresponding author on reasonable request.

REFERENCES

Arnaud K. A., 1996, in Jacoby G. H., Barnes J., eds, ASP Conf. Ser. Vol. 101, Astronomical Data Analysis Software and Systems V. Astron. Soc. Pac., San Francisco, p. 17
Bondi H., 1952, MNRAS, 112, 195
Chakrabarti S., Titarchuk L. G., 1995, ApJ, 455, 623
Chakrabarti S. K., 1989, ApJ, 347, 365
Chakrabarti S. K., 1990, Theory of Transonic Astrophysical Flows. World Scientific Publishing Co, Singapore
Chakrabarti S. K., 1996a, MNRAS, 283, 325
Chakrabarti S. K., 1996b, ApJ, 471, 237
Chakrabarti S. K., Das S., 2001, MNRAS, 327, 808
Chakrabarti S. K., Khanna R., 1992, MNRAS, 256, 300
Chakrabarti S. K., Molteni D., 1993a, ApJ, 417, 671
Chakrabarti S. K., Molteni D., 1993b, ApJ, 417, 671
Chakrabarti S. K., Mondal S., 2006, MNRAS, 369, 976
Chakrabarti S. K., Acharyya K., Molteni D., 2004, A&A, 421, 1
Chakrabarti S. K., Mondal S., Debnath D., 2015, MNRAS, 452, 3451
Das S., Chattopadhyay I., Chakrabarti S. K., 2001, ApJ, 557, 983
Das S., Chattopadhyay I., Nandi A., Molteni D., 2014, MNRAS, 442, 251
Deb A., Giri K., Chakrabarti S. K., 2016, MNRAS, 462, 3502
Debnath D., Chakrabarti S. K., Mondal S., 2014, MNRAS, 440, L121
Debnath S., Chattopadhyay I., Joshi R. K., 2024, MNRAS, 528, 3964
Dihingia I. K., Das S., Maity D., Chakrabarti S., 2018, Phys. Rev. D, 98, 083004
Eze A. C., Eze R. N. C., Chukwude A. E., Madu F. O., 2025, Sci. Rep., 15, 11556
Fukue J., 1987, PASJ, 39, 309
Garain S. K., 2025, Astron. Comput., 53, 100974
Garain S. K., Kim J., 2023, MNRAS, 519, 4550
Garain S. K., Ghosh H., Chakrabarti S. K., 2012, ApJ, 758, 114
Garain S. K., Ghosh H., Chakrabarti S. K., 2014, MNRAS, 437, 1329
Garain S. K., Balsara D. S., Chakrabarti S. K., Kim J., 2020, ApJ, 888, 59
Giri K., Chakrabarti S. K., Samanta M. M., Ryu D., 2010, MNRAS, 403, 516
Gu W.-M., Foglizzo T., 2003, A&A, 409, 1
Gu W.-M., Lu J.-F., 2006, MNRAS, 365, 647
Hawley J. F., Smarr L. L., Wilson J. R., 1984, ApJS, 55, 211
Kim J., Garain S. K., Balsara D. S., Chakrabarti S. K., 2017, MNRAS, 472, 542
Kim J., Garain S. K., Chakrabarti S. K., Balsara D. S., 2019, MNRAS, 482, 3636
Lee S.-J., Ryu D., Chattopadhyay I., 2011, ApJ, 728, 142
Lee S.-J., Chattopadhyay I., Kumar R., Hyung S., Ryu D., 2016, ApJ, 831, 33
Mao J., Dihingia I. K., Mizuno Y., Nagataki S., 2025, ApJ, 990, 12
Misner C. W., Thorne K. S., Wheeler J. A., 2017, Gravitation. Princeton University Press, New Jersey, p. 639
Molla A. A., Chakrabarti S. K., Debnath D., Mondal S., 2017, ApJ, 834, 88
Molteni D., Lanzafame G., Chakrabarti S. K., 1994, ApJ, 425, 161
Molteni D., Ryu D., Chakrabarti S. K., 1996, ApJ, 470, 460
Molteni D., Tóth G., Kuznetsov O. A., 1999, ApJ, 516, 411
Molteni D., Gerardi G., Teresi V., 2006, MNRAS, 365, 1405
Mondal S., Basu P., 2020, MNRAS, 497, 2119
Mondal S., Chakrabarti S. K., 2006, MNRAS, 371, 1418
Mukhopadhyay B., 2002, ApJ, 581, 427
Nagakura H., Yamada S., 2008, ApJ, 689, 391
Nagakura H., Yamada S., 2009, ApJ, 696, 2026
Nakayama K., 1992, MNRAS, 259, 259
Nakayama K., 1994, MNRAS, 270, 871
Nandi P., Chatterjee A., Chakrabarti S. K., Dutta B. G., 2021, MNRAS, 506, 3111
Nath S. K., Debnath D., Chatterjee K., Bhowmick R., Chang H.-K., Chakrabarti S. K., 2024, ApJ, 960, 5
Nobuta K., Hanawa T., 1994, PASJ, 46, 257
Okuda T., Molteni D., 2012, MNRAS, 425, 2413
Okuda T., Teresi V., Molteni D., 2007, MNRAS, 377, 1431
Olivares H. R., Mościbrodzka M. A., Porth O., 2023, A&A, 678, A141
Paczyński B., Wiita P. J., 1980, A&A, 88, 23
Proga D., Begelman M. C., 2003a, ApJ, 582, 69
Proga D., Begelman M. C., 2003b, ApJ, 592, 767
Ryu D., Brown G. L., Ostriker J. P., Loeb A., 1995, ApJ, 452, 364
Ryu D., Chakrabarti S. K., Molteni D., 1997, ApJ, 474, 378
Shakura N. I., Sunyaev R. A., 1973, A&A, 24, 337
Shang J. R., Debnath D., Chatterjee D., Jana A., Chakrabarti S. K., Chang H. K., Yap Y. X., Chiu C. L., 2019, ApJ, 875, 4
Shapiro S. L., Teukolsky S. A., 1983, Black holes, White Dwarfs and Neutron Stars. The Physics of Compact Objects. John Wiley and Sons, Inc., New York, p. 347
Suková P., Charzyński S., Janiuk A., 2017, MNRAS, 472, 4327
Wilson J. R., 1972, ApJ, 173, 431

APPENDIX A: FORCE ANALYSIS

In this section, we analyse the net force distribution to support the claim that the outflows in our simulations are generated from centrifugal and pressure gradient forces. For this analysis, we choose a case with flow parameters $\epsilon = 0.0061$ and $l = 1.66$. For this set of parameters, the flow profile is smooth with a clear standing shock and nearly steady outflow from the post-shock region. The two components of the net force, F_R and F_Z (see equation 9), are as follows:

$$F_R = \frac{v_\phi^2}{R} - \frac{1}{\rho}\frac{\partial P}{\partial R} - \frac{\partial \Phi}{\partial r}\frac{R}{r}, \quad \text{(A1)}$$

$$F_Z = -\frac{1}{\rho}\frac{\partial P}{\partial Z} - \frac{\partial \Phi}{\partial r}\frac{Z}{r}. \quad \text{(A2)}$$

These force components are computed at each grid point. Fig. A1 presents a comparative picture of the (a) net force field and the corresponding (b) velocity field, both overplotted with the $\log_{10}\rho$ distribution. The length of an arrow is proportional to the logarithmic magnitude of the vector in both plots. We show a zoomed-in region [0:10] × [0:10] in these plots. The region bounded by the white circle in Fig. A1(a) shows the force field away from the black hole. The corresponding velocity field shows that matter is getting accelerated outward from this region. Since this case shows mostly a steady solution, the velocity vectors towards upper part of the white circle are already accelerated to nearly a steady velocity by this steady force field.

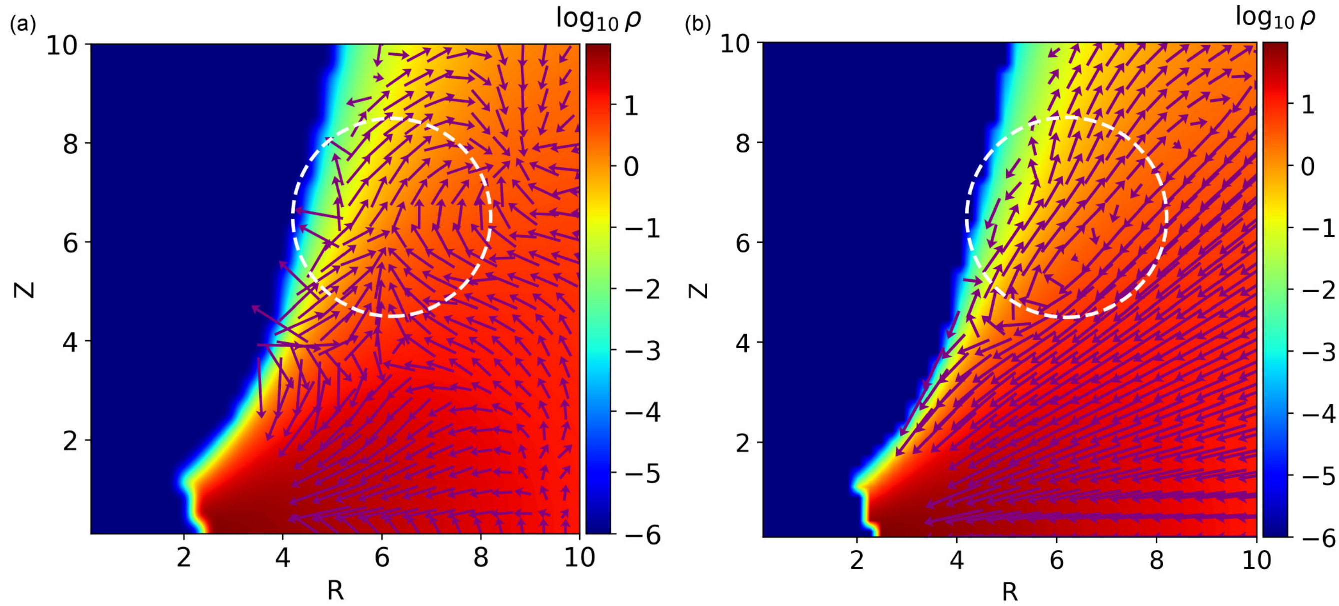

Figure A1. Show (a) net force vectors and (b) velocity field plotted over $\log_{10}\rho$ distribution for a point from the shock region. The region bounded by the white circle in (a) shows the force field away from the black hole. The corresponding velocity field in (b) shows that matter is getting accelerated outward from this region.

This paper has been typeset from a TEX/LATEX file prepared by the author.